



Heriot-Watt University  
Research Gateway

## Dynamic Fluid Ingress Detection in Geomaterials using K-band Frequency Modulated Continuous Wave Radar

### Citation for published version:

Blanche, J, Lewis, H, Couples, GD, Buckman, J, Lenoir, N, Tengattini, A & Flynn, D 2020, 'Dynamic Fluid Ingress Detection in Geomaterials using K-band Frequency Modulated Continuous Wave Radar', *IEEE Access*, vol. 8, pp. 111027-111041. <https://doi.org/10.1109/ACCESS.2020.3002147>

### Digital Object Identifier (DOI):

[10.1109/ACCESS.2020.3002147](https://doi.org/10.1109/ACCESS.2020.3002147)

### Link:

[Link to publication record in Heriot-Watt Research Portal](#)

### Document Version:

Publisher's PDF, also known as Version of record

### Published In:

IEEE Access

### General rights

Copyright for the publications made accessible via Heriot-Watt Research Portal is retained by the author(s) and / or other copyright owners and it is a condition of accessing these publications that users recognise and abide by the legal requirements associated with these rights.

### Take down policy

Heriot-Watt University has made every reasonable effort to ensure that the content in Heriot-Watt Research Portal complies with UK legislation. If you believe that the public display of this file breaches copyright please contact [open.access@hw.ac.uk](mailto:open.access@hw.ac.uk) providing details, and we will remove access to the work immediately and investigate your claim.

Received April 24, 2020, accepted June 6, 2020, date of publication June 12, 2020, date of current version June 25, 2020.

Digital Object Identifier 10.1109/ACCESS.2020.3002147

# Dynamic Fluid Ingress Detection in Geomaterials Using K-Band Frequency Modulated Continuous Wave Radar

JAMIE BLANCHE<sup>1</sup>, (Member, IEEE), HELEN LEWIS<sup>2</sup>, GARY D. COUPLES<sup>2</sup>,  
JIM BUCKMAN<sup>2</sup>, NICOLAS LENOIR<sup>3,4</sup>, ALESSANDRO TENGATTINI<sup>3,4</sup>,  
AND DAVID FLYNN<sup>1</sup>, (Member, IEEE)

<sup>1</sup>Smart Systems Group, Heriot-Watt University, Edinburgh EH14 4AS, U.K.

<sup>2</sup>Institute of Geoenergy Engineering, Heriot-Watt University, Edinburgh EH14 4AS, U.K.

<sup>3</sup>Laboratoire 3SR, CNRS, Grenoble INP, Université Grenoble Alpes, 38400 Saint-Martin-d'Hères, France

<sup>4</sup>Institut Laue-Langevin (ILL), 38000 Grenoble, France

Corresponding author: Jamie Blanche (j.blanche@hw.ac.uk)

This work was supported in part by the Energy Technology Partnership (ETP) and Maersk/Total S. A. under Grant ETP 87/B12S10307, in part by the EPSRC Project under Grant B16R12502, and in part by the Laboratoire 3SR through the NeXT-Grenoble Project funded by the French National Research Agency in the framework of the Investissements d'avenir Program under Grant ANR-15-IDEX-02.

**ABSTRACT** Frequency modulated continuous wave (FMCW) radar in the K-band has been shown to be an effective detector of geomaterial physical properties being highly sensitive to rock characteristics, particularly mineral composition and, for porous rock, variations in liquid water content. This research demonstrates that contrasts in FMCW return signals with time correlate with changes in geomaterial water content. FMCW signal returns were acquired for porous sandstone samples subjected to controlled water injection while also in a neutron beam, taking advantage of the well-known, and well-calibrated, attenuation of neutrons by hydrogen atoms for the water-containing porous sandstone samples. The sequential neutron tomographic images clearly show water moving up the sample with time while the FMCW observations show increases in radar reflection coefficient as a function of water position in the field of view. The observed FMCW detection of flood-front position is corroborated by the synchronous neutron tomographic images. We also observe repeatable variations in the radar reflection coefficient as a function of sample orientation during fluid injection, verifying that FMCW sensing offers real-time insight into the interactions between fluid movement and sample heterogeneity, via non-contact and non-invasive flood-front tracking. This research demonstrates that FMCW has potential to be a more accessible and easily deployable sensing modality than neutron tomography, enabling dynamic geomaterial testing to be conducted outwith the confines of the highly controlled laboratory environment required for neutron investigation.

**INDEX TERMS** Geologic measurements, rock porosity, microwave propagation, non-destructive testing, radar applications, radar measurements, neutron tomography.

## I. INTRODUCTION

One current matter of considerable societal importance is the need for a complex multi-objective optimization of environmental objectives, energy security and energy equity [1]–[3]. This approach mirrors the wider need to optimize all subsurface energy source uses, recognizing benefits, costs and consequences. Many repercussions arise from the disposal of by-products and wastes from our energy sources.

The associate editor coordinating the review of this manuscript and approving it for publication was Xiaokang Yin<sup>1</sup>.

Burning fossil fuels, both coal and petroleum, create wastes and by-products, including CO<sub>2</sub>, produced water and airborne particulates. Nuclear energy creates wastes as part of the extraction of uranium, and the spent fuel plus the reactor facilities wastes must be isolated. These examples and others have direct links to the subsurface which can be both the source and the repository over both shorter (months to decades) and longer (millennia) timeframes. Waste isolation involves considering the movement of subsurface fluids through the rocks that contain them. So, research streams focused on fluid flow processes that occur naturally, and those caused

by humans, are equally significant, and are the subject of this research.

As is well understood, the rocks that comprise much of the accessible subsurface have voids that are remnant spaces between particles, together with fractures and zones where solid material has been dissolved. These voids are typically sub-micron to millimetre in size but can be larger. The subsurface, and particularly its void spaces, provide many exploitation opportunities. Natural fluids including potable water, briny waters with valuable dissolved chemicals and petroleum can be extracted via drilled boreholes. The voids can serve as storage space for industrial fluids and in some situations, fluids are both injected and extracted in the same operation to extract heat or chemicals. So, fluids and fluid movements within rocks are common factors in most human interactions. The subsurface rock system, from near-surface tunneling for aquifer withdrawals, nuclear waste subsurface storage or disposal, require the drilling of boreholes to depths that range from 10 metres to 10 kilometres for geothermal heat extraction, petroleum recovery, CO<sub>2</sub> storage, and mining. Natural processes can induce beneficial fluid movements or induce hazards, such as slope failures. They can deliver hazardous substances into the biosphere or trigger earthquakes. In short, fluids within subsurface rocks are important but unseen elements that have broad impacts on social and economic matters.

Engineers and scientists exploiting the subsurface need to characterize the geomaterials to develop an understanding of how their properties, particularly at the small scale, govern fluid flow processes, both naturally active and induced [4]–[14]. Laboratory studies play key roles in developing that understanding for both the geomaterial framework [15] and the contained fluids [16], [17]. Laboratory studies also support the derivation of behavioural laws that underpin numerical simulations of the subsurface [18], [19], to performing the numerical simulations themselves and thus provide understanding of unseen processes [20]. A large body of work already provides general understanding and associated laws. However, as the subsurface uses are progressively required to be more efficient, for example to include rock damage prediction, including of sealing units [21]–[24], or to have higher levels of safety, the remaining questions lead researchers to continue probing the processes involved in fluid movement and its interactions with the rock petrophysical properties, including deformed-rock petrophysical properties [7].

The most well-developed application area, where the flow properties of rocks are economically important, has historically been in the petroleum industry. There, reservoir rocks and their seals (rocks with much lower fluid transmissibility) have been intensively studied for decades, with a strong focus on both the rock properties and how fluids move [4], [6]–[8], [11]–[14], [16], [17]. That expertise has translated to CO<sub>2</sub> storage [5], [18], [19], with which it has a great deal in common, and also to geothermal energy [25]–[27] and nuclear waste storage [28], [29]. Characterizing the

void-space of a rock is an essential component in the effective management and operation of a subsurface process. This involves description and quantification of void-space distribution and connectivity; identifying the presence, magnitude and distributions of fracturing; and deriving estimates or measurements of the fluid flow characteristics (petrophysical properties) of the multiple rock-property elements within the subsurface domain. The studies noted above have contributed substantially to developing the required knowledge base but are typically hampered by the difficulty of obtaining 3D solid-pore and pore fluid distributions. With advancing technology, it becomes possible to obtain full-volume characterizations of samples from the rock mass, especially focused on imaging its void system, such as with X-ray tomographic methods [30], including multi-phase fluid positions and distributions by using a dopant while X-ray tomographic experiments using a synchrotron can capture extremely fast processes [31]. Direct *in situ* imaging of fluid flow processes can be imaged using neutron tomography [13], [16] while synchronous use of X-ray and neutron imaging methods can detect fully-registered rock framework and fluid distributions [32].

Neutron radiography and tomography are particularly useful because of neutron sensitivity to hydrogen, allowing clear images of water movements through a rock. Neutrons interact far less with the rock materials, allowing the water in the images to stand out clearly. Using two forms of water, D<sub>2</sub>O (heavy water) and H<sub>2</sub>O, the contrasting interactions of these hydrogen isotopes with neutrons allow tracking of fully-saturated water flow processes, along with water-air exchanges [17], [33]. However, access to neutron facilities is extremely limited, focused on short-duration access restricting the number of experiments that can be performed, with further issues involving specialist sample preparation and the inability to customize the neutron method into a front-line detection systems or dynamic environment testing. This paper describes a new imaging tool that has the potential to contribute to laboratory studies of fluid movement through rocks. Our results and analysis show that Frequency Modulated Continuous Wave radar (FMCW), which operates as a non-destructive and external imaging system is able to detect contrasting fluid phases that move through rocks in 3D, and to track the change of fluid phase position with time. The significance of this new imaging method is that it adds to the set of full-volume imaging techniques, with the potential that a combination of tools can be deployed within a laboratory setting to provide a means of observing fluid flows without being fully dependent on limited-access facilities like a neutron beam facility. This paper addresses the ability of FMCW to detect water invasion of air-dry porous sandstones in 3D with time, both undeformed and laboratory pre-deformed, testing the accuracy of the FMCW sensitivity to water incursion, while being benchmarked by concurrent neutron tomographic image acquisition. The FMCW method also reduces experiment costs and offers versatility in application and deployment without significant compromise of

accuracy or sensitivity. This method also provides dynamic laboratory understanding as well as the prospect of in-field deployment customization.

This research is a further development of the geomaterial analytical technique developed by Blanche *et al.* 2018 [34], which demonstrated the potential to detect the presence of deionized water, and sample mineralogical and physical characteristics, using a K-band monostatic radar configuration. We conduct a programme that adds new sensing tools to the suite of methods used to assess geomaterials, placing emphasis on the impact of this work being not only the discovery of a new tool for geomaterial analysis, but also exploring if new, dynamic measurands may be analysed, via low cost, and low maintenance sensing in real-time. Potentially this approach and technology can provide insight into the observed behaviours of these materials, but confidence in its reliability requires it to be corroborated and benchmarked by advanced neutron analyses. This series of experiments, performed at the Institut Laue-Langevin (ILL), were designed to evaluate the accuracy of the novel FMCW sensing modality, with the most advanced laboratory method, to verify the ability of the radar measurands to detect variation in signal to water abundance.

The paper is structured as follows; Section II outlines previous work in the novel use of FMCW for the analysis of geomaterials, providing background for the current work. Section III discusses the application of FMCW to dielectric media. Section B presents equipment and geomaterial characterization, with section IV/A outlining antenna characterization work, and section IV/B providing an analysis of geomaterial constituents and fabric. Section V outlines the experimental setup; with the data acquisition procedure during fluid invasion presented in section V/A. Section VI presents the X-ray, neutron beam and FMCW results acquired during this study. Section VII presents a discussion of the results and section VIII lists conclusions.

## II. PREVIOUS WORK

Due to advancements in the miniaturization of microwave electronics, FMCW has been deployed in environmental applications to detect variations in stratigraphic features in snow deposition, allowing regions of variable density, porosity and fluid saturation to be identified by measuring water equivalence by volume [35], [36]. With most devices used in this role being in the X-Band (8-12 GHz), and with a bistatic antenna configuration being the norm, the size and weight of an experimental setup was significant until recent advances in the miniaturization of FMCW electrical hardware [37], [38]. The work reported here, using such miniaturized equipment, demonstrates the capability of FMCW to determine pore-fluid (in this case water) presence and, where possible, to estimate local fluid phase saturations within deformed and undeformed sandstone samples.

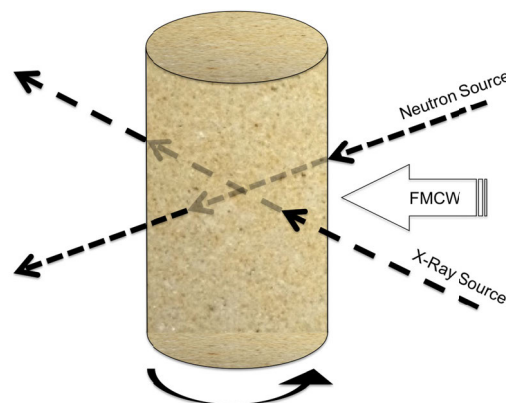


**FIGURE 1.** Orthogonal beam incidences onto rotating cylindrical sandstone samples within NeXT-Grenoble Chamber at ILL. Note that the detectors are outwith this view.

### A. ANALYSIS OF GEOMATERIALS USING FMCW RADAR

Recent advances in full field geomaterial analysis via the application of FMCW radar have shown that this K-band configuration can detect experimentally-created deformation features in rocks that have passed their yield point, damaging the rock, often by breaking and shearing the grains and their cement [39]. This damage, developed in semi-planar finite-width zones, alters porosity (and hence density) as well as particle sizes, roundness, and the spatial density of interfaces. FMCW has also been shown to detect the presence of fluids and fluid type, within porous media. High-dielectric inclusions can also be detected [34], [40], [41].

Neutron tomography is an excellent indicator of water-air front position and of qualitative, and sometimes-quantitative measures of the pore (and fracture) system water saturation. FMCW sensing represents a functional addition to current full-field measurement techniques. In this paper, liquid injection experiments are performed on both Darny and Red St Bee's sandstones. Both experimentally deformed and undeformed cylinders were tested in the NeXT-Grenoble/D50 apparatus at the Institut Laue-Langevin (ILL) neutron beamline in Grenoble (France) [42]. This instrument has the capability for X-ray acquisition synchronous with neutron acquisition. These experiments involve injecting water into air-dry porous sandstone cylinders rotating in the neutron beam. In detail the experiments use controlled-rate water injection at the jacketed cylindrical sample base, while the sample was rotated 360° in the neutron beamline and where a radially incident orthogonally placed X-ray beam was used to acquire radiography datasets needed for subsequent neutron and X-ray tomographic reconstructions (Figure 1). In this way, simultaneous, time-stamped datasets of FMCW signal return, and X-ray and neutron images, were acquired during water invasion into the air-dry samples to confirm that FMCW can identify water presence. This corroboration versus the neutron analysis verifies that the FMCW can be used a replacement for neutron tomography both in the laboratory and in the field. Within section III,

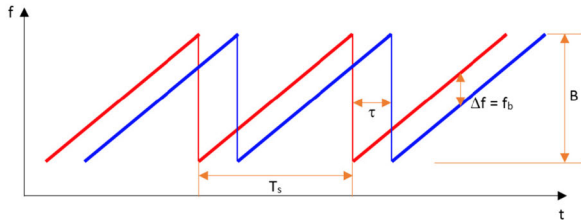


**FIGURE 2.** “Sawtooth” Tx and Rx signals from FMCW module, where  $f$  = frequency,  $t$  = time,  $T_s$  = sweep duration,  $\tau$  = two way travel time of return signal,  $B$  = sweep bandwidth and  $\Delta f$  = intermediate frequency [28].

we introduce FMCW theory and outline the application of microwave sensing in the K-band to geomaterial analysis.

### III. RADAR AND DIELECTRIC THEORY

FMCW represents a continuous wave output and thus differs from commonly used, higher power, pulsed-wave radars. Frequency modulation of the continuous wave provides a frequency shift over time to create a saw-tooth (or triangular) frequency output, as shown in Figure 2. A difference in frequency between the transmitted and received signals is determined by the convolution of output and input waveforms to give a new, lower- frequency signal, which can be analysed to calculate the distance and velocity of an object. The difference in frequency observed between output and received signals is calculated and transmitted to a data logger as an intermediate frequency (IF) signal of frequency  $\Delta f$ . An overview of the determination of the IF signal of frequency  $\Delta f$  is as follows:

$$f_{RF_{out}} = f_{RF_0} + k_f \times t \tag{1}$$

where  $0 \leq t \leq T$ ,  $f_{RF_0}$  is the starting frequency,  $T$  is the frequency sweep and  $k_f$  is the sweep rate.

$$k_f = \frac{B}{T} \tag{2}$$

where,  $B$  is the frequency bandwidth for the sweep and with the two-way time (TWT) of the emitted signal calculated as:

$$\Delta t = 2 \frac{d}{c} \tag{3}$$

where  $d$  is the distance between the antenna and the reflecting target and  $c$  is the speed of light in the medium of propagation. Therefore, due to the observed delay in return signal, the return frequency compared to the emitted frequency will be:

$$f_{RReceived} = f_{RF0} + k_f * (t - \Delta t) \tag{4}$$

where,  $\Delta t \leq t \leq T + \Delta t$ . The difference in frequency ( $\Delta f$ ) between the emitted and received signal is therefore:

$$\Delta f = k_f * (-\Delta t) \tag{5}$$

It is this difference in frequency that is output as data by the sensor. The negative time of flight can be taken as a magnitude, allowing for the expression:

$$\Delta f = \frac{B}{T} * 2 \frac{d}{c} \tag{6}$$

Due to the relationship expressed in equation (6), distance between the sensor and geomaterial sample is kept constant. Thereby, any signal variation can be attributed to the geomaterial intrinsic properties, and dynamic changes, such as fluid influx. Defining a “free space” measurement as the determination of the reflection coefficient of a target medium via the properties of a return signal mediated by air (or a vacuum), FMCW operating in normal mode (perpendicular to target) represents a non-contact means for target property analysis. This section outlines the theory that allows for the calculation of the target reflection coefficient via amplitude and frequency responses to the active radar. Equation (7) represents the complex component form of  $\epsilon_r^*$ , the complex relative electrical permittivity of a particular medium.  $\epsilon'$  represents the observed and “real” permittivity of the material in an idealized form. The imaginary component,  $i\epsilon''$ , denotes the “loss factor” of the material and therefore represents the dispersion of incident radiation due to conduction and relaxation of atomic constituents.

$$\epsilon_r^* = \epsilon' + i\epsilon'' \tag{7}$$

In many theoretical instances, the complex aspect of this relationship is ignored, as materials used for dielectric media tend to be poor conductors (i.e. low  $i\epsilon''$ ). However, applications within geomaterial samples could be contrary to this assumption, with many constituent parts of a geomaterial matrix and void spaces offering appreciable conduction, for example, the presence of water/brines, other fluids, and mineral inclusions [43]. Nevertheless, as an initial assessment, this study operates under the assumption that the component of dielectric loss, the imaginary term  $i\epsilon''$ , in equation (7), is much smaller than the real component (and thus that term is eliminated) that represents the reflection data.

The following term for the reflection coefficient,  $\Gamma$ , equation (8) can be derived from incident and reflected wave equations.

$$\Gamma = \frac{I_{reflected}}{I_{incident}} = \frac{(\eta_1 - \eta_2)^2}{(\eta_1 + \eta_2)^2} \tag{8}$$

where  $I$  is the intensity of the incident signal. Calculation of the reflection coefficient requires the determination of the refractive index of the target material,  $\eta_2$ . This can be achieved via analysis of the reflection coefficient,  $\Gamma$ , of the target material, as determined by taking the ratio of the reflected signal amplitude over the incident signal amplitude (or ideal reflectance) to give  $\Gamma$ , as shown in equation (8). In practice, quantification of the incident radiation amplitude can be achieved by analysis of the signal return from an ideal reflector: a smooth surface with very high electrical conductivity oriented normal to the direction of signal propagation.

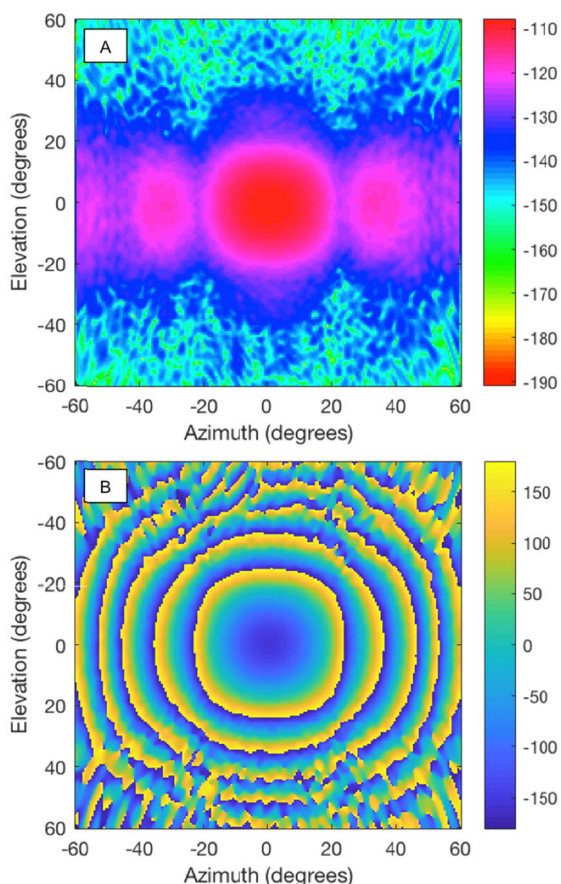


**FIGURE 3.** A) 2D amplitudinal radiation pattern for K-Band Flann Microwave antenna model 21240-20 (Scale bar in dBm). B) 2D phase shift radiation pattern for K-Band Flann Microwave antenna model 21240-20 (Scale bar in Degrees).

For the experimentation described throughout this document, a smooth, solid steel cylinder was used. For simplicity, this work will present the radar signal return amplitude as the dimensionless reflection coefficient,  $\Gamma$ .

**IV. EXPERIMENTAL PROCEDURE AND SAMPLE PREPARATION**

**A. ANTENNA CHARACTERIZATION**

To obtain an appropriate geomaterial response for a Flann K-band antenna model: #21240-20/serial: #219405, a vector network analyser (VNA) output is set to represent a bandwidth sweep of 1.5 GHz. To meet this requirement, three scans were performed using a two-dimensional translation stage coupled to an OEWG (open-ended waveguide) standard probe, type WR42, for the K- band (18-26.5 GHz) and using a non-radiative near-field separation distance between the probe and the antenna under test (AUT) of 100 mm. Data sets were acquired representing the 1500 MHz bandwidth sweep for the frequency band. Figure 3A shows the radiation pattern acquired, and both 2D and 3D representations are shown. Figure 3B illustrates the phase shift characteristic of this antenna. The Flann Microwave antenna displays a

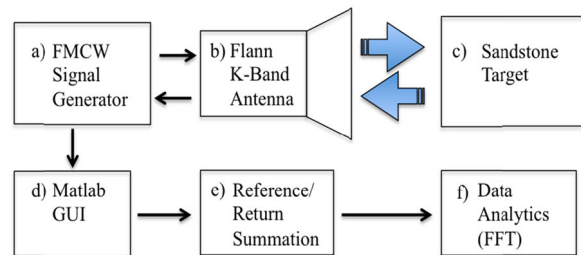


**FIGURE 4.** Block diagram of experimental setup showing hardware components and analytical procedure.

dispersal characteristic with a peak amplitude spot size on the target found to be  $\sim 36.4$  millimetres radius at a separation of 100 mm with a minimal phase differential, representing the effective sample window. The value of this work is that in all subsequent experimentation utilizing this antenna configuration, the sample area under scrutiny can be quantified as being within the consistent radius of  $\sim 36.4$  millimetres, if all work is conducted at a sample/antenna distance of 100 mm. Figure 4 shows a block diagram of the experimental setup and procedure, which can be divided into 6 main stages:

- a) FMCW signal generator providing a waveform with a bandwidth from 24 – 25.5 GHz and with chirp duration of 300 milliseconds,
- b) Flann Microwave model 21240-20 standard gain horn antenna (serial number 219405) for radiation output 17.6 - 26.7 GHz and with a nominal gain of 20 dBi (at 22.15 GHz). This antenna was affixed to a static mounting and directed onto the sandstone samples maintaining a separation distance of 100 millimetres,
- c) Cylindrical samples of Darney and Red St. Bee’s sandstones,
- d) Graphical User Interface via Matlab 2018a,
- e) Summation of reference and return signal waveforms to generate intermediate frequency (IF),
- f) Data analysis via Fourier transform into frequency domain, from which amplitude extractions are performed. Calculation of the reflection coefficient was achieved via the ratio of the radiation intensity peak,  $I_{\text{incident}}$ , measured for the control sample (steel cylinder acting as an ideal reflector) and the radiation return signal,  $I_{\text{reflected}}$ , acquired by the K-band antenna [44], as outlined in equation (8).

**B. MATERIAL OVERVIEW**

Both sandstones are used as building stones and have been well characterized by the supplier [45], [46], with additional work performed by [34] and [39]. The Darney sandstone consists predominantly of moderately well-sorted, sub-angular quartz ( $\text{SiO}_2$ ) grains, of fine to medium grain size (125 – 350  $\mu\text{m}$ ), with subsidiary orthoclase feldspar and clay (kaolinite), with a typical porosity of 18.7% [47]. Figure 5A is a composite false colour image overlaying the relative magnitudes of characteristic X-rays for selected elements onto

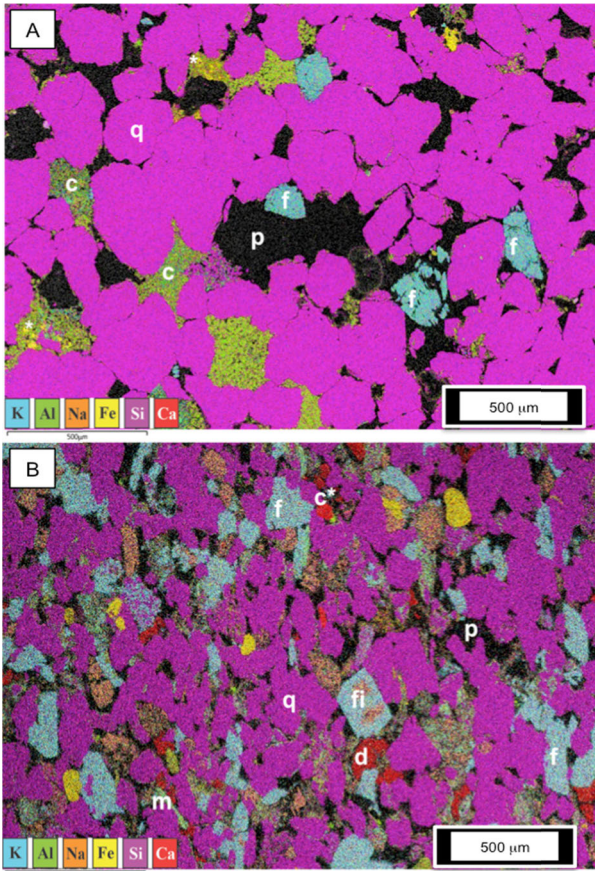


**FIGURE 5.** A) Energy dispersive X-ray false colour composite image of Darney sandstone. B) Energy dispersive X-ray false colour composite image of Red St. Bee's sandstone. Scale bar (bottom left each image) is 500  $\mu\text{m}$ . Key ) p = pore, q = quartz, f = feldspar, c = clay, \* = iron-rich particles, m = mica, c\* = calcium phosphate, d = dolomite, fi = feldspar with intergrowths.

electron backscatter images obtained via energy dispersive X-ray techniques, as previously reported in [34]. Assigned colours represent each detected chemical element, with dark regions representing pore-spaces. The orthoclase feldspar can be identified as distinct, angular, and often fractured or cleaved grains, rich in aluminium and potassium. This sample is relatively free of high permittivity metallic inclusions that would affect the apparent dielectric strength, however, Figure 5A illustrates the presence of iron within some kaolinite-filled/lined pores. Figure 5A, a backscattered electron (BSE) image displaying material greyscale contrast due to atomic number, shows variability in grainsize (note length scale is common to Figure 5 and Figure 6), porosity, metallic clay content and iron-rich particles. Figure 7A shows the high definition gaseous secondary electron (GSE) image of the sample showing original grains, mostly quartz, in grey with the cement in very pale grey.

Both undeformed and laboratory-deformed rocks are tested, with a set consisting of eight cylinder-shaped samples of diameter 38 mm and length 76 mm cored from blocks of Darney and Red St. Bee's sandstones. Four cylinders were extracted from each sandstone block, and two of

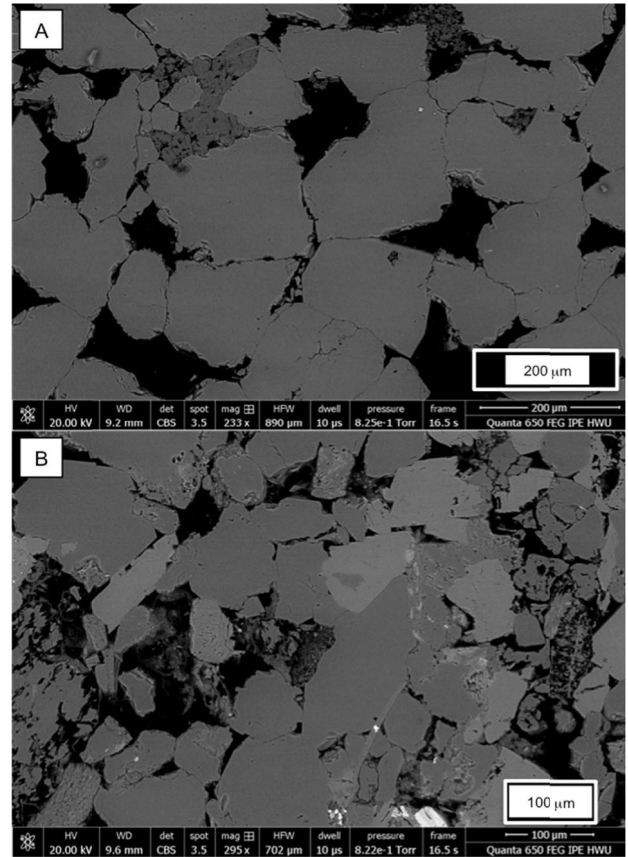


**FIGURE 6.** A) Backscattered Electron (BSE) image of Darney sandstone. Scale bar is 200  $\mu\text{m}$ . B) Backscattered Electron (BSE) image of Red St. Bee's sandstone. Scale bar is 100  $\mu\text{m}$ .

each type was deformed to induce localized damage. The deformed samples were loaded uniaxially (unconfined) by a computer-controlled hydraulic press until immediately after initial yield [39]. Note that the arrangement did not provide lateral confinement due to the requirement for microwave transparency: impossible within a metallic pressure vessel. In the unconfined experiments described here, applied force and axial displacement were recorded in order to calculate axial stress and strain responses.

The Darney sandstone can be considered as the most mineralogically pure sample used in this study, being strongly quartz-dominant and with a very small proportion of diagenetic kaolinite or other minerals, including very few metallic mineral inclusions. Where present, the metallic components are concentrated in discrete thin films at grain boundaries, typically held within the kaolinite-filled portions of pores. With well-cemented sub-angular grains that have no dominant crystallographic orientation, this sandstone is homogeneous from an incident microwave radiation perspective.

The Red St. Bee's sandstone sample displays a larger variety of minerals and displays significant laminae, very thin depositional layering, from which high heterogeneity for incident microwave radiation is inferred. Unpolarized and plane-polarized optical microscope imagery of a rock thin section, a 30-micron thick rock sliced and mounted on a

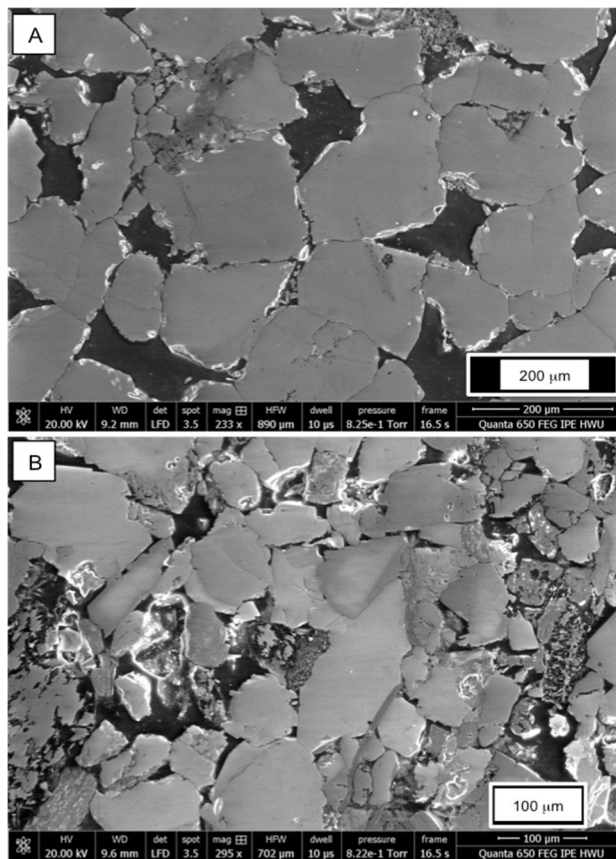


**FIGURE 7.** A) Gaseous Secondary Electron (GSE) image of Darney sandstone. Scale bar is 200 μm. B) Gaseous Secondary Electron (GSE) image of Red St. Bee's sandstone. Scale bar is 100 μm.

glass slide, shows that the Red St. Bee's exhibits no common grain long-axis orientation. With sub-angular to sub-rounded, very-fine to fine-sized grains (50 – 200 μm) and a porosity of 21.3% [47], this sample has a notably diverse mineralogy and contains the highest levels of metallic elements for potassium, calcium, sodium and aluminium (confirming the presence of both orthoclase and plagioclase feldspars in addition to abundant clays). Figure 5B strongly supports the presence of mica, calcium phosphate and dolomite, the last being calcium and magnesium carbonate. The elements iron, magnesium and titanium are also present in measurable quantities (Table 1). Figure 6B, a high-definition BSE image, illustrates the highly angular quartz grains, feldspar grains with feldspar overgrowths and pore-filling clays. Some feldspar overgrowths are also clearly visible in GSE imagery (Figure 7B) in addition to the formation of secondary porosity due to identification of feldspar weathering or “rotten feldspar”. Table 2 outlines known rock properties for both sandstones taken from the technical data sheets provided by Marshall-Stancliffe Stones [45], [46] and from observation via optical, X-ray and SEM microscopy.

**V. EXPERIMENTAL WORK**

The basic principle of tomography is to record sequential radiographies, each of which is a 2D projection of the

**TABLE 1.** EDX derived atomic weight percentages for the Darney and Red St. Bee's sandstone samples.

%	Darney	Red St. Bee's
Carbon	43.9	42.6
Oxygen	42.4	42.5
Silicon	12.9	12.2
Aluminium	0.7	1.3
Potassium	0.1	0.5
Iron	<0.1	0.2
Magnesium	<0.1	0.2
Calcium	<0.1	0.1
Sodium	<0.1	0.2
Titanium	<0.1	~0.1

attenuated signal (here of neutrons or X-rays) as it passes through the sample onto a single plane, and to do this at multiple angles around a symmetry axis so that the set of 2D images can be inverted to create a tomographic image. The set of radiographies is reconstructed into a 3D image using so-called “reconstruction algorithms” based on the Radon transform. See [17] and [30] for a thorough description of the neutron and X-ray techniques respectively. NeXT-Grenoble is a new Neutron and X-ray imaging instrument inaugurated in 2016 from the joint effort of Université Grenoble Alpes, UGA (and specifically Laboratoire 3SR) and the ILL. It takes advantage of the world-leading neutron flux provided by the ILL nuclear reactor, which automatically makes this a unique instrument in terms of performances. A key feature of the instrument is the possibility to perform simultaneous X-ray and neutron tomography during *in situ* testing, in order to take advantage of the high complementarity of the attenuation coefficients of these two techniques [42].

Specifically here, both neutrons and X-rays are used, the neutrons because of their hydrogen sensitivity, and hence, water-detection capabilities within partially-saturated targets, and the X-rays because they provide a high-resolution image of the porous rock microstructure [48]. Previous work by the author has detected the presence of liquids within a porous sample, via non-invasive and non-destructive millimetre wave interrogation, demonstrating that the presence of (even trace, volumes of) liquid water or kerosene are visible to FMCW radar in both the X and K-bands [34], [40], [41] and, if all other factors are known via baseline measurement, the magnitude of fluid ingress may be inferred by analysis of the reflection co-efficient in free space (non-contact) conditions. By repeating these tests in the neutron beam, we take advantage of the high sensitivity of the neutrons to hydrogen to image in 3D the evolution of the water-air-front when a known volume of H<sub>2</sub>O is injected at a known rate. Prior to these studies, FMCW has not been used to detect the physical characteristics of rocks and their contained fluids.

The Darney Sandstone was selected for the uniformity and relative homogeneity observed in static tests outlined in [34], [40], [41]. With a well-understood matrix and granular constituent mineralogy, this rock represents the best-case

**TABLE 2.** Key characteristics of the Darney and Red St. Bee’s sandstones. Summarized from technical data sheets provided by stone supplier and laboratory observation.

Geomaterial Property	Darney Sandstone [45]	Red St. Bee’s Sandstone [46]
Open Porosity, $\phi$ (%)	18.7	21.3
Apparent Density, $\rho$ (kg/m <sup>3</sup> )	2150	2090
Geological Age	Lower Carboniferous Sandstone	Permo-Triassic Sandstone
Approximate Provenance Area	Darnley Quarry, Northumberland	Birkhams Quarry, Cumbria
Colour/Texture	Pale Gold, yellow cream - light buff - fine to medium grained	Dark Red/Fine to medium grained
Water Absorption (% by wt)	5.3	6.8
Water absorption by capillarity (g/m <sup>2</sup> /s)	192.7	75.76
Grain Size, Sorting	Medium (lower) 0.25 – 0.35 mm Moderately to well sorted	Fine to Medium <0.177 – 0.35 mm Well sorted within fine laminae
Grain Morphology	Spheroidal, Sub rounded-rounded	Spheroidal, Sub angular-sub rounded.
Grain Orientation	No common orientation	No common orientation
Mineralogy	Quartz dominated	Quartz dominated
Matrix/Grain	Grain supported, well cemented with some quartz overgrowth	Grain supported with little or no observed matrix
Deformation and weathering	Evidence of granular fracture	Evidence of granular fracture
Notes	Relative abundance of mineral inclusions	Well defined fine-grained laminae alternating red to pink with some lamina of medium grain

scenario for tracking a dynamic flood front within the NeXT-Grenoble environment.

The Red St. Bee’s Sandstone was selected due to its much more heterogeneous composition with high heterogeneity including its layered nature. The Red St. Bee’s sandstone contains visible laminae of variable permeability, grain size, morphology and mineralogical composition. It was expected that these laminae would act as baffles, reducing fluid flux due to their more-complex pore space characteristics, and that these effects would be detected.

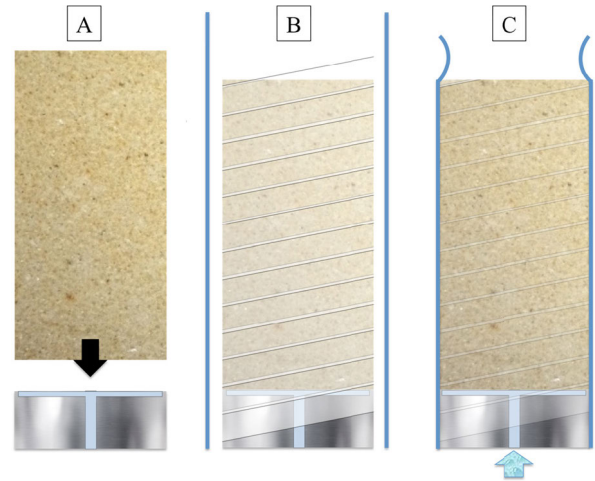


**FIGURE 8.** Schematic of sandstone mounting technique. A: Sample placed onto injection base, which has a large-diameter open space to distribute water across the sample end. B: Base and sample wrapped in Teflon PTFE tape and heat shrink jacket placed over assembly. C: Heat is applied to shrink JACKET; Assembly is sealed and water ingress is only possible via end cup injection port at bottom of sample.

The following sections outline the dynamic FMCW response acquired during fluid invasion experiment at the neutron beamline at ILL.

**A. FMCW EXPERIMENTAL DESIGN FOR INVASION BY FLUIDS IN NEUTRON AND X-RAY BEAMS**

The experimental setup required synchronous recording of neutron, X-ray and FMCW data (illustrated in Figure 1), while water was injected at a controlled rate at the base of a jacketed sample and collected in a reservoir at the top of the sample. Most of the experimental assembly was completed prior to placing the sample in the experimental chamber. The methods follow those described by Lewis et al (2020) [49]. In order to regulate the flow of fluids from sample base to top, the assembly included an end cup placed at the base, containing a small reservoir, which distributed the water across the sample base (Figure 8A). After being placed on the end cup, the sample and end cup were wrapped in PTFE/teflon tape (Figure 8B), and then heat-shrink jacketed. The jacket was left 3 cm longer than the sample at the top to create space for water that had passed through the sample to accumulate (Figure 8C). The purpose of the shrink-wrap and PTFE tape were to prevent fluid passage along the sample exterior and, thus, the cylinder sides were no-flow boundaries. The jacketed sample was placed in the chamber with the beam off (shutter closed), centred on the rotation stage and fixed in place. The water supply was then attached, and all fittings checked prior to the removal of all persons from the chamber. The neutron beam shutter was opened and radiography was continuously monitored and recorded throughout the experiment. All experiments were conducted at room temperature with the FMCW antenna placed 10 cm from the sample surface and out of line of both the neutron and the X-ray

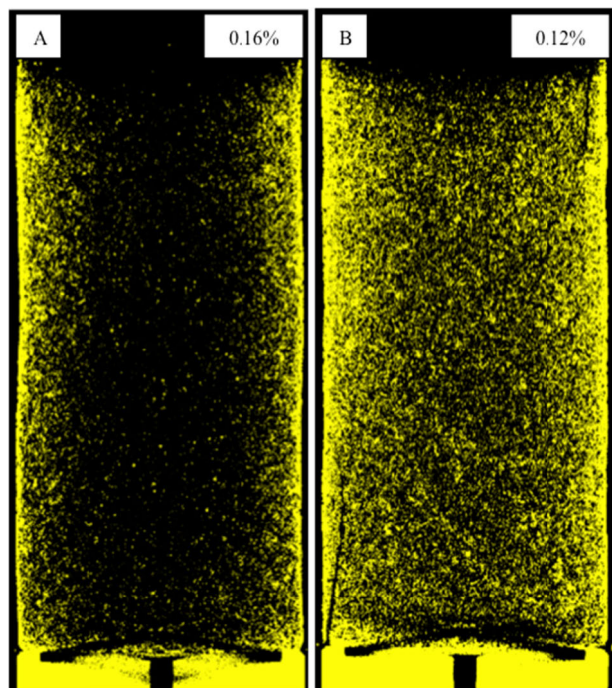


**FIGURE 9.** Vertical slices taken from X-ray reconstruction and segmentation prior to fluid injection. Yellow represents high permittivity material. A: Darney 1 BC (undeformed) sample, B: Darney 2 B (deformed) sample.

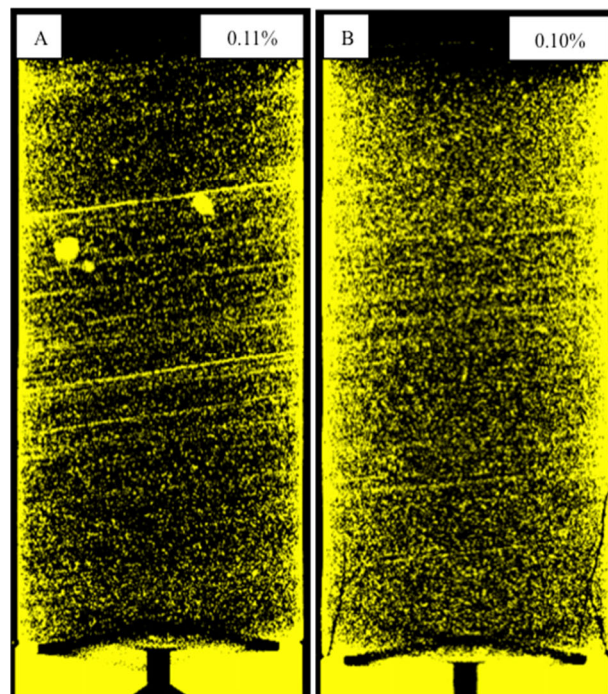


**FIGURE 10.** Vertical slices taken from X-ray reconstruction and segmentation prior to fluid injection. Yellow represents high permittivity material. A: Red St. Bee's 1TC (undeformed) sample and B: Red St. Bee's 2T (deformed) sample.

**TABLE 3.** Parameters for neutron data acquisition.

Parameter	Value (unit)
Number of Images per rotation	600
Geometrical Zoom	1.09
Optical Zoom	0.05
Voxel Size	96.05 $\mu\text{m}$
Volume Height	98.1 $\mu\text{m}$
Slices	1021

beams. Shielding was used as practical to minimize antenna and waveguide exposure to radiation. All tests used deionized H<sub>2</sub>O, with a controlled injection rate of 0.5 ml/minute, which results in a sample base water pressure of approximately 10kPa. Neutron data acquisition parameters are given in Table 3. Each test took approximately 6 hours to set up and perform, with several hours additional cool-down time to allow for radioactive decay (of activated elements) to return gamma emissions to a safe level. All experiments occurred in the following sequence:

- 1) Air-dry X-ray 360° tomography with no introduced water, with reconstructed images shown in Figure 9 for the Darney sandstone samples and Figure 10 for the Red St. Bee's sandstone samples,
- 2) Air-dry neutron 180° tomography with FMCW while the sample is rotating for the record of radiographies,

in order to determine the radar sensitivity to orientation and to set a dynamic baseline for each sample (radar return data is shown in Figure 11),

- 3) Introduction of water at sample base during the simultaneous acquisition of consecutive 180° neutron and 360° X-ray tomographies and with FMCW radar returns recorded (Figure 12 and Figure 13)

## VI. X-RAY, NEUTRON AND FMCW RESULTS

The capability of neutron investigation to detect water that is present in open fractures is visible in Figure 12 (lower sequence) for Darney sandstone sample 2B, where the fracture leads to localized regions of higher water saturation.

For the Red St. Bee's samples and the observed presence of laminae, the expectation is that the variation in vertical hydraulic permeability that is inherent in a stacked package of laminae, will result in episodic upwards movement of the water front, where fluid pressure driven water movement and spontaneous imbibition are both active. This is particularly well illustrated in Figure 13 [lower sequence] for Red St. Bee's sample 2T, where it can be noted that the water front adopts a planar shape once it moves away from the end. Changes in fluid proximity to the sensor correlate to an increase in observed reflection coefficient as the fluid enters the field of view of the sensor, and this is observed in all sandstone samples tested. Figure 15 and Figure 16 show the correlation between the neutron tomography imagery acquired during tests. Each half rotation (180°) of the sample

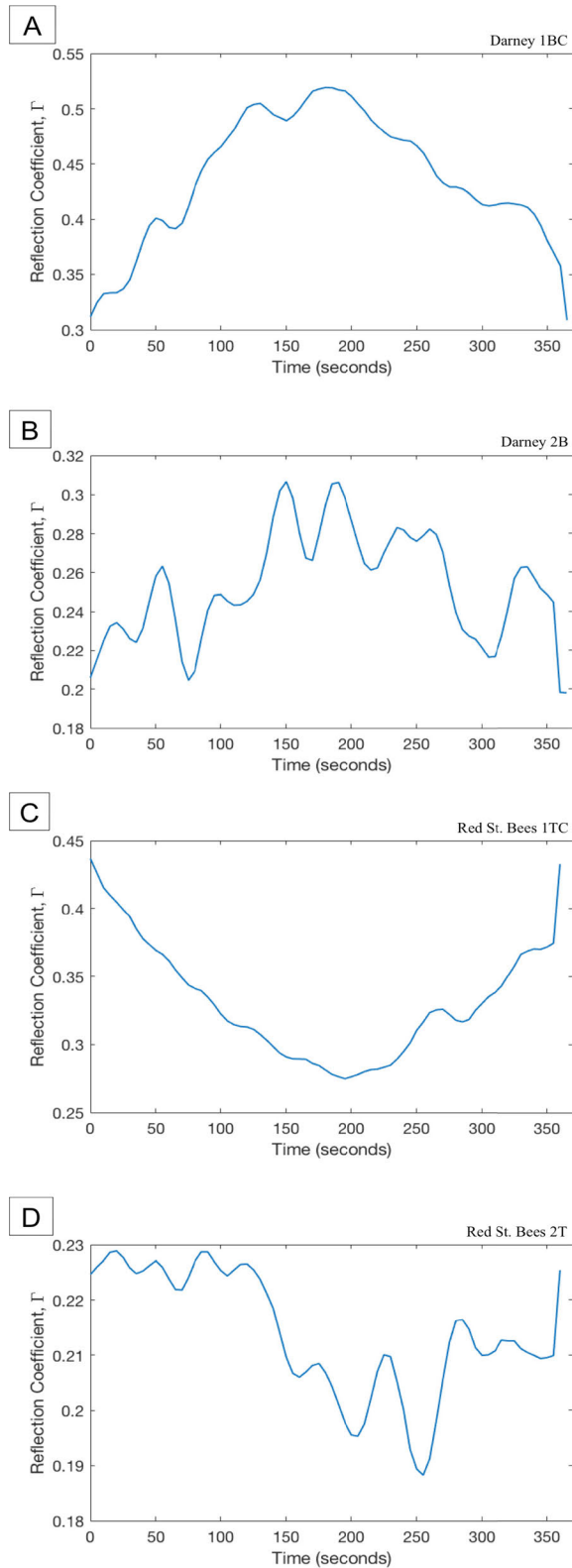


**FIGURE 11.** A) Reflection coefficient vs. time for sample DARN1BC. B) Reflection coefficient vs. time for sample DARN2B. C) Reflection coefficient vs. time for sample RSB1TC. D) Reflection coefficient vs. time for sample RSB2T. All plots taken at bin #48 for one half rotation (180°) within the beamline.

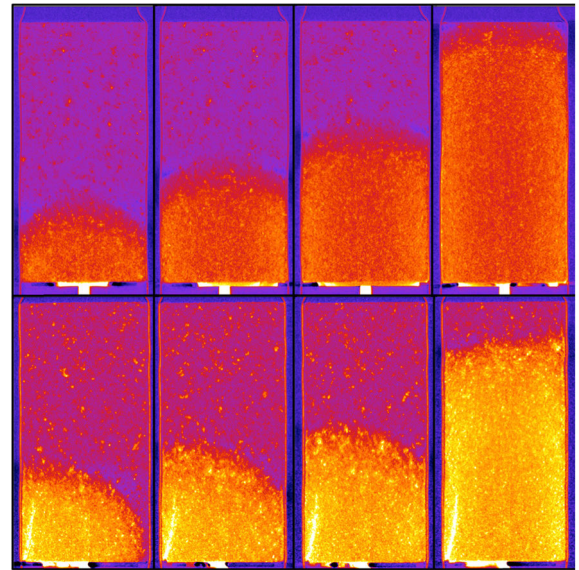


**FIGURE 12.** Darney sample neutron vertical slice tomography acquisitions during fluid injection from sample base. Upper row = Darney Sandstone 1BC. Lower row = Darney Sandstone 2B (deformed, see fracture lower left).

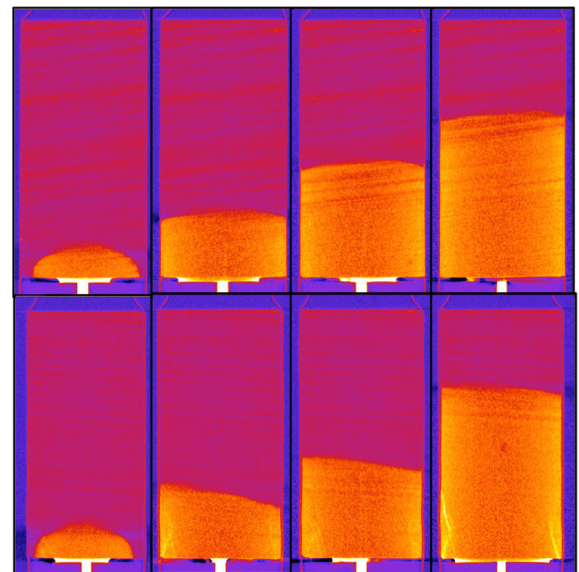


**FIGURE 13.** Red St. Bee's sample neutron vertical slice tomography acquisitions during fluid injection from sample base. Upper row = Red St. Bee's Sandstone 1TC. Lower row = Red St. Bee's Sandstone 2T (deformed, see fractures at bottom of sample).

took 360 seconds (6 minutes) at a rate of 30° per minute, where the radiographies are acquired on the return rotation.

**A. DARNEY SANDSTONE SAMPLE 1 BC (UNDEFORMED)**

For the undeformed Darney 1BC sample (Figure 15A), 8 rotations were completed (totaling ~45 minutes in the beamline). FMCW data for rotation 000 was found to be corrupt, resulting in a loss of data for the first rotation. There is also a notable anomaly for the first tomographic acquisition for the Darney 1BC sample. It is not clear why the

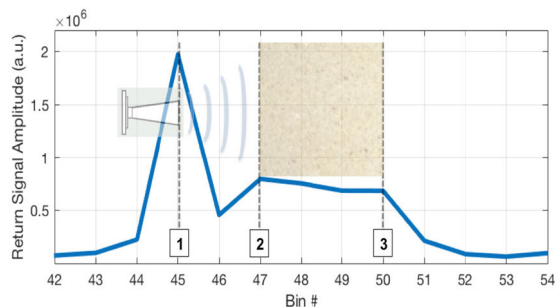


**FIGURE 14.** Frequency domain transform of FMCW return data: point 1 is the antenna coupling, point 2 is the first sample interface (entry into sandstone cylinder) and point 3 is the second sample interface (exit from sandstone cylinder).

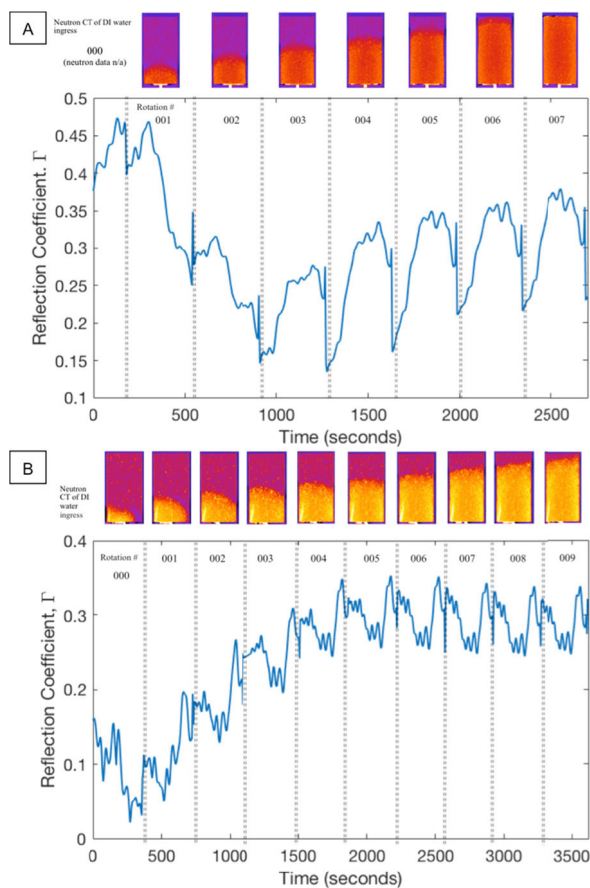


**FIGURE 15.** A) Reflection coefficient,  $\Gamma$ , acquired via FMCW return signal versus time for the Darney 1BC sample (undeformed). B) Reflection coefficient,  $\Gamma$ , acquired via FMCW return signal versus time for the Darney 2B sample (deformed). Each sample rotation is shown with inset neutron tomography acquisition detailing the progression of the deionized water flood front through the sample.

observed reflection coefficient,  $\Gamma$ , for tomography 000 started at  $\sim 0.4$  and peaked at  $\sim 0.47$ , prior to dropping to  $\sim 0.15$  at the end of tomography 002. Beyond rotation 002, the  $\Gamma$  for this sample follows a trend that is more in keeping with the deformed Darney sample 2B, with an observed increase in  $\Gamma$  as a function of deionized water volume uptake, with the maximum  $\Gamma$  value observed to be  $\sim 0.35$ , occurring at the

maximum level of partial water saturation. X-ray analysis of this sample allows for the quantification of the highest reflection coefficient constituent materials present in the sample, allowing for an understanding for the distribution of metals within the sample and the mapping of magnesium, aluminium and iron-rich particles. Adjusting the threshold of the imaging software [50] used to generate the maps shown in Figure 9, reveals that the volumetric percentage of high permittivity materials within the field of view of the FMCW sensor is approximately 0.16%.

**B. DARNEY SANDSTONE SAMPLE 2B (DEFORMED)**

For the deformed Darney 2B sample (Figure 15B), 10 tomographies were completed (totaling  $\sim 58$  minutes in the beamline). All FMCW datasets for this sample were found to be useable and the observed trend shows that, where the water was not within the field of view of the FMCW sensor,  $\Gamma$  was found to be between  $\sim 0.02$  and  $\sim 0.16$  and varies as a function of sample orientation relative to the sensor, correlating with the baseline established in Figure 11. As the water entered the field of view of the sensor, the observed  $\Gamma$  can be seen to steadily increase, while continuing to vary as a function of orientation. These values of  $\Gamma$  correlate with those acquired for the Darney 1BC sample, with only marginally lower maximum  $\Gamma$  values observed for this sample. Using the same analytical technique employed for Darney sample 1TC, ImageJ software determined that the volumetric percentage of high permittivity materials within the field of view of the FMCW sensor is approximately 0.12%.

**C. RED ST. BEE'S SANDSTONE SAMPLE 1TC (UNDEFORMED)**

For the undeformed Red St. Bee's 1TC sample (Figure 16A), 17 tomographies were completed (totaling  $\sim 102$  minutes in the beamline). This sample exhibits the largest variation in  $\Gamma$  as a function of orientation, with a range between  $\sim 0.25$  and  $\sim 0.43$ . This cyclic trend is highly consistent and is believed to be a result of the high variability in mineral distribution observed in this sample during characterization work. This sample, due to its different petrophysical properties, has a lower permeability than the Darney sandstone samples, as evidenced by the longer time for a fluid front to pass through the sample under the same injection rate conditions. However, a steady reflection coefficient may be observed that is consistent with the presence of water and the progression of the air-water front across the field of view of the sensor, clearly visible in the neutron tomography images. The highest  $\Gamma$  value, representing the maximum partial water saturation within the field of view, is  $\sim 0.59$ , where the highest corresponding  $\Gamma$  value for the minimum partial water saturation is  $\sim 0.36$ . As used in both previously analysed Darney samples, the use of ImageJ software with X-ray data determined that the volumetric percentage of high permittivity materials within the field of view of the FMCW sensor is approximately 0.11% for this sample.

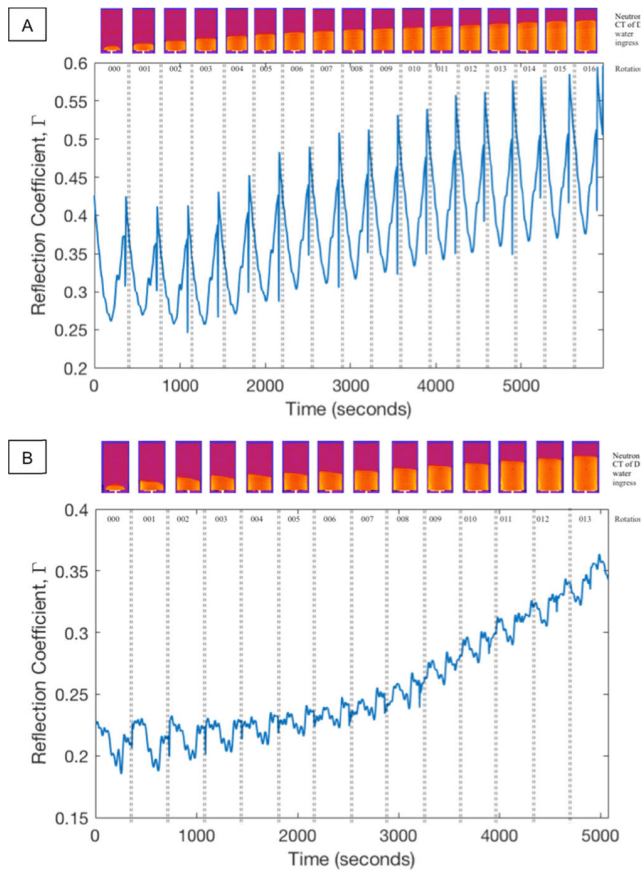


**FIGURE 16.** A) Reflection coefficient,  $\Gamma$ , acquired via FMCW return signal versus time for the Red St. Bee's 1T sample (undeformed). B) Reflection coefficient,  $\Gamma$ , acquired via FMCW return signal versus time for the Red St. Bee's 2T sample (deformed). Each sample rotation is shown with inset images of neutron data detailing the progression of the deionized water front through the sample.

**D. RED ST. BEE'S SANDSTONE SAMPLE 2T (DEFORMED)**

For the deformed Red St. Bee's 2T sample (Figure 16B), 14 tomographies were completed (totaling ~84 minutes in the beamline). The variation between the maximum and minimum return signal for this sample is the lowest of all the samples tested in this beamline experiment, with the lowest readings for  $\Gamma$  (taken just as fluid uptake had commenced) ranging between ~0.17 and 0.23. The continued influx of water from the sample base, leads to a commensurate rise in observed  $\Gamma$  to a maximum value of ~0.36 (representing the maximum partial saturation value at the cessation of the experiment). The issue of calibrating water partial saturations in samples is an active consideration for the range of experiments being conducted at ILL. Note also that the volumetric percentage of high permittivity materials is approximately 0.10% for this sample.

**VII. DISCUSSION**

The purpose of this research is to corroborate the observed rate-controlled injection and progression of a deionized H<sub>2</sub>O fluid front, during injection (Figure 12 and Figure 13) at a controlled rate, through the Darney and Red St.

Bee's sandstones. The further purpose is to identify whether K-band FMCW may also detect water front variations caused by the damage-induced increase or decrease of porosity in sub-millimetre width fractures and deformation bands. The FMCW was set to transmit and receive a single chirp of 300 milliseconds duration, and of bandwidth 1500 MHz (24 – 25.5 GHz), once every 5 seconds. These settings provide a spatial resolution of approximately 1 cm in a vacuum or in air [51], resulting in a region of the Fourier transformed return signal representing an internal view of the sandstone samples. Performing a fast Fourier transform (FFT) allows for a representative distance measurement, where each bin number can be quantified as approximately the spatial resolution of the sensor. However, consideration must be given to the change in electromagnetic propagation velocity within the geomaterial samples and compensation must be made for this reduction in velocity that results in a concurrent reduction in spatial resolution. These observations are described in Figure 14 where the antenna response (due to a right angle bracket) is visible at bin #45 (point 1), and the first target interface is visible at bin #46-47 (point 2). Bins #47-50 represent the internal structure of the sandstone sample and bins #50 and #51 (point 3) represent the exit interfaces of the sample.

For the all results interpreted within this paper, bin #48 has been utilized to represent the central region of the sandstone samples during study. By analysis of the radar return signal, a free space measurement is acquired and interrogated to infer a reflection coefficient value for the bulk material that is visible in the radar antenna field of view (FOV). At 100 millimetres distance to target, FOV is 100 mm<sup>2</sup> for the antenna used. Amplitudinal data for the first radar contact (the sandstone targets) has been interpreted via comparison to an ideal reflector held at the same range from the antenna (in this work a steel cylinder of the same dimensions to the sandstone samples) to give a reflection coefficient,  $\Gamma$ . The observed reflection coefficient is calculated and plotted in Figure 15 and Figure 16 for both sandstone samples, in both undeformed and deformed states, as a function of experimental runtime.

The Darney Sandstone is known to contain very few metallic inclusions and consequently, gives a “clean” signal return, where the mean baseline reflects the presence of H<sub>2</sub>O with a higher value than a less partially saturated section of rock. The cyclic nature of the FMCW returns in all plots is indicative of possible variations in:

- Sample distance to the antenna due to non-central placement on the rotation stage
- Variations in clast orientation and layering as a function of rotation
- Variations in position of high permittivity inclusions entering/leaving the bulk field of view within the sample during rotation

For the Red St. Bee's samples, it is proposed that the higher overall reflection coefficient determinations for the undeformed sample versus the deformed sample may be due an abundance of high permittivity inclusions present, that are

not present in such abundance for the deformed sample. Such variation is expected for rocks of this type.

### VIII. SUMMARY AND CONCLUSION

Undeformed and previously experimentally deformed porous sandstone samples are studied using the NeXT-Grenoble instrument and imaged by both neutrons and X-rays in order to generate tomographic images. Each polymer-jacketed sample was injected with deionized H<sub>2</sub>O to generate a flood front through the sample, and to study the effects of the intrinsic pre- and post- deformation rock properties on the flow of fluids resulting from an applied pressure gradient. Each sample was mounted on a rotation stage that turned the sample at a fixed rate relative to the beams and radiographic images were collected at closely spaced intervals. This allowed for the reconstruction of tomographic data to create a digital 3D volume for later analysis. The X-ray tomographic volume gives the solid rock framework and the neutron tomographic volume allows the determination of the changing, sequential positions of deionized water. This experimental procedure is the current state of the art with regard to the study of fluid flow through a deformed (or undeformed) The use of FMCW in conjunction with these experimental procedures is a novel and valuable application of the technology and represents a new tool for the analysis of rock properties. This work has resulted in the following observations:

- It is possible to detect the presence of water within a geomaterial sample with FMCW,
- It is possible to determine changes in the amount of water as a function of time (and thus space) and, consequently, it is possible to track a flood-front within the field of view of the sensor,
- It is also possible to detect heterogeneity and anisotropic effects within a sample as a function of axial rotation.

The experimental results of the FMCW analysis, verified via neutron beam tomography, demonstrates that this technology provides a valuable means of identifying pore-space occupancies within partially water-saturated sandstones as well as the ability to quantify certain geomaterial properties, including mineralogy and porosity variation resulting from deformation and composition. The presence of deionized water within the sandstone samples is clearly discernable, as are the textural changes caused by previous laboratory-induced deformation on the rate of fluid progression through the sample from the X-ray tomography. This research has demonstrated that the detection of a localized region of dilatant deformation (sample Darney 2B) corresponds to an increased fluid front progression rate under a known constant applied pressure gradient. This study has also shown that the detection of a localized region of compactive deformation (sample Red St. Bee's 2T) corresponds to a decreased rate of movement for a fluid (Table 4). Future work will focus on continued dynamic real-time analysis of geomaterials in which we intend to further exploit the benefits of a non-contact and non-destructive means of tracking pore occupancies, porosity

**TABLE 4. Summary of observations from FMCW combined with neutron tomography conducted at Institut Laue-Langevin.**

Sample	$\Gamma$	$\phi$	Deformation
Darney 1BC	$\sim 0.13 - \sim 0.47$	baseline	none
Darney 2B	$\sim 0.02 - \sim 0.35$	> baseline	dilatant
Red St. Bee's 1TC	$\sim 0.25 - \sim 0.59$	baseline	none
Red St. Bee's 2T	$\sim 0.17 - \sim 0.36$	< baseline	compactive

changes and high permittivity mineral presence. Further validation of FMCW analysis under dynamic loading conditions would be a significant advance for the geoscientist and geomechanicist, which can augment current tomographic methods.

The application of FMCW in this role, therefore, offers a means to contribute to the refinement of geomechanical modelling techniques currently employed to develop the understanding of fluid/pore network interaction, albeit at lower resolution than the one offered by the neutron and X-ray tomographic methods but with the benefit of a wider range of scales of observation. The availability of multi-scale measurements is generally seen as a benefit and not a detrimental addition. The sensitivity of this sensing modality, and its non-contact and non-destructive properties, have the potential to provide near to real-time analysis of geomaterials under varying test conditions and to inform the creation of more accurate geomechanical modelling by allowing for more portable initial investigation equipment.

### ACKNOWLEDGMENTS

The authors wish to thank the Energy Technology Partnership (ETP) and Maersk/Total S. A. for providing project funding, and James Somerville of the Institute of Geoenery Engineering, Heriot-Watt University, for his technical assistance. Jamie Blanche and Helen Lewis also thank the NeXT-Grenoble project supported by the French National Research Agency, for neutron beam access and funding.

### REFERENCES

- [1] M. Andoni, V. Robu, and D. Flynn, "Crypto-control your own energy supply," *Nature*, vol. 548, no. 7666, p. 158, 2017, doi: [10.1038/548158b](https://doi.org/10.1038/548158b).
- [2] V. Robu, D. Flynn, M. Andoni, and M. Mokhtar, "Consider ethical and social challenges in smart grid research," *Nature Mach. Intell.*, vol. 1, no. 12, pp. 548–550, Dec. 2019, doi: [10.1038/s42256-019-0120-6](https://doi.org/10.1038/s42256-019-0120-6).
- [3] C. Etukudor, B. Couraud, V. Robu, W.-G. Früh, D. Flynn, and C. Okereke, "Automated negotiation for Peer-to-Peer electricity trading in local energy markets," *Energies*, vol. 13, no. 4, p. 920, Feb. 2020, doi: [10.3390/en13040920](https://doi.org/10.3390/en13040920).
- [4] A. Hosa, R. A. Wood, P. W. M. Corbett, R. S. De Souza, and E. Roemers, "Modelling the impact of depositional and diagenetic processes on reservoir properties of the crystal-shrub limestones in the 'Pre-Salt' Barra Velha formation, Santos Basin, Brazil," *Mar. Petroleum Geol.*, vol. 112, Feb. 2020, Art. no. 104100, doi: [10.1016/j.marpetgeo.2019.104100](https://doi.org/10.1016/j.marpetgeo.2019.104100).
- [5] N. Kampman, P. Bertier, A. Busch, J. Snippe, J. Harrington, V. Pipich, A. Maskell, and M. Bickle, "Validating reactive transport models of CO<sub>2</sub>-brine-rock reactions in caprocks using observations from a natural CO<sub>2</sub> reservoir," *Energy Procedia*, vol. 114, pp. 4902–4916, Jul. 2017, doi: [10.1016/j.egypro.2017.03.1632](https://doi.org/10.1016/j.egypro.2017.03.1632).

- [6] B. Zhao, C. W. MacMinn, B. K. Primkulov, Y. Chen, A. J. Valocchi, J. Zhao, Q. Kang, K. Bruning, J. E. McClure, and C. T. Miller, "Comprehensive comparison of pore-scale models for multiphase flow in porous media," *Proc. Nat. Acad. Sci. USA*, vol. 116, no. 28, pp. 13799–13806, Jul. 2019, doi: [10.1073/pnas.1901619116](https://doi.org/10.1073/pnas.1901619116).
- [7] Z. Jiang, G. D. Couples, H. Lewis, and A. Mangione, "An investigation into preserving spatially-distinct pore systems in multi-component rocks using a fossiliferous limestone example," *Comput. Geosci.*, vol. 116, pp. 1–11, Jul. 2018, doi: [10.1016/j.cageo.2018.04.004](https://doi.org/10.1016/j.cageo.2018.04.004).
- [8] Z. Jiang, M. I. J. van Dijke, S. Geiger, J. Ma, G. D. Couples, and X. Li, "Pore network extraction for fractured porous media," *Adv. Water Resour.*, vol. 107, pp. 280–289, Sep. 2017, doi: [10.1016/j.advwatres.2017.06.025](https://doi.org/10.1016/j.advwatres.2017.06.025).
- [9] H. Andr a, N. Combaret, J. Dvorkin, E. Glatt, J. Han, M. Kabel, Y. Keehm, F. Krzikalla, M. Lee, C. Madonna, M. Marsh, T. Mukerji, E. H. Saenger, R. Sain, N. Saxena, S. Ricker, A. Wiegmann, and X. Zhan, "Digital rock physics benchmarks—Part I: Imaging and segmentation," *Comput. Geosci.*, vol. 50, pp. 25–32, Jan. 2013, doi: [10.1016/j.cageo.2012.09.005](https://doi.org/10.1016/j.cageo.2012.09.005).
- [10] H. Andr a, N. Combaret, J. Dvorkin, E. Glatt, J. Han, M. Kabel, Y. Keehm, F. Krzikalla, M. Lee, C. Madonna, M. Marsh, T. Mukerji, E. H. Saenger, R. Sain, N. Saxena, S. Ricker, A. Wiegmann, and X. Zhan, "Digital rock physics benchmarks—Part II: Computing effective properties," *Comput. Geosci.*, vol. 50, pp. 33–43, Jan. 2013, doi: [10.1016/j.cageo.2012.09.008](https://doi.org/10.1016/j.cageo.2012.09.008).
- [11] M. J. Blunt, B. Bijeljic, H. Dong, O. Gharbi, S. Iglauer, P. Mostaghimi, A. Paluszny, and C. Pentland, "Pore-scale imaging and modelling," *Adv. Water Resour.*, vol. 51, pp. 197–216, Jan. 2013, doi: [10.1016/j.advwatres.2012.03.003](https://doi.org/10.1016/j.advwatres.2012.03.003).
- [12] T. Bultreys, W. De Boever, and V. Cnudde, "Imaging and image-based fluid transport modeling at the pore scale in geological materials: A practical introduction to the current state-of-the-art," *Earth-Sci. Rev.*, vol. 155, pp. 93–128, Apr. 2016, doi: [10.1016/j.earscirev.2016.02.001](https://doi.org/10.1016/j.earscirev.2016.02.001).
- [13] K. Singh, B. U. Anabaraonye, M. J. Blunt, and J. Crawshaw, "Partial dissolution of carbonate rock grains during reactive CO<sub>2</sub>-saturated brine injection under reservoir conditions," *Adv. Water Resour.*, vol. 122, pp. 27–36, Dec. 2018, doi: [10.1016/j.advwatres.2018.09.005](https://doi.org/10.1016/j.advwatres.2018.09.005).
- [14] C. Soulaire, S. Roman, A. Kovscek, and H. A. Tchelepi, "Mineral dissolution and wormholing from a pore-scale perspective," *J. Fluid Mech.*, vol. 827, pp. 457–483, Sep. 2017, doi: [10.1017/jfm.2017.499](https://doi.org/10.1017/jfm.2017.499).
- [15] J. Desruets, P. B esuelle, and H. Lewis, "Strain localization in geomaterials," *Geological Soc., London, Special Publications*, vol. 289, no. 1, pp. 47–73, 2007, doi: [10.1144/SP289.4](https://doi.org/10.1144/SP289.4).
- [16] G. Wang, G. E. Pickup, K. S. Sorbie, and E. J. Mackay, "Detailed assessment of compositional and interfacial tension effects on the fluid behaviour during immiscible and near-miscible CO<sub>2</sub> continuous and WAG displacements," *Transp. Porous Media*, vol. 131, no. 3, pp. 805–830, Feb. 2020, doi: [10.1007/s11242-019-01368-x](https://doi.org/10.1007/s11242-019-01368-x).
- [17] E. Tudisco, M. Etxegarai, S. A. Hall, E. M. Charalampidou, G. D. Couples, H. Lewis, A. Tengattini, and N. Kardjilov, "Fast 4-D imaging of fluid flow in rock by high-speed neutron tomography," *J. Geophys. Res., Solid Earth*, vol. 124, no. 4, pp. 3557–3569, Apr. 2019.
- [18] J. Rutqvist, D. W. Vasco, and L. Myer, "Coupled reservoir-geomechanical analysis of CO<sub>2</sub> injection and ground deformations at in Salah, Algeria," *Int. J. Greenhouse Gas Control*, vol. 4, no. 2, pp. 225–230, Mar. 2010.
- [19] H. Rattez, I. Stefanou, and J. Sulem, "The importance of thermo-hydro-mechanical couplings and microstructure to strain localization in 3D continua with application to seismic faults. Part I: Theory and linear stability analysis," *J. Mech. Phys. Solids*, vol. 115, pp. 54–76, Jun. 2018.
- [20] H. Lewis, S. A. Hall, and G. D. Couples, "Geomechanical simulation to predict open subsurface fractures," *Geophys. Prospecting*, vol. 57, no. 2, pp. 285–299, Mar. 2009, doi: [10.1111/j.1365-2478.2009.00786.x](https://doi.org/10.1111/j.1365-2478.2009.00786.x).
- [21] H. Lewis, P. Olden, and G. D. Couples, "Geomechanical simulations of top seal integrity," in *Norwegian Petroleum Society Special Publications*, vol. 11. Amsterdam, The Netherlands: Elsevier, 2002, pp. 75–87.
- [22] M. Rouainia, H. Lewis, C. Pearce, N. Bicanic, G. D. Couples, and M. A. Reynolds, "Hydro-geomechanical modelling of seal behaviour in overpressured basins using discontinuous deformation analysis," *Eng. Geol.*, vol. 82, no. 4, pp. 222–233, Feb. 2006, doi: [10.1016/j.enggeo.2005.11.004](https://doi.org/10.1016/j.enggeo.2005.11.004).
- [23] E.-M. Charalampidou, S. A. Hall, S. Stanchits, H. Lewis, and G. Viggiani, "Characterization of shear and compaction bands in a porous sandstone deformed under triaxial compression," *Tectonophysics*, vol. 503, nos. 1–2, pp. 8–17, Apr. 2011, doi: [10.1016/j.tecto.2010.09.032](https://doi.org/10.1016/j.tecto.2010.09.032).
- [24] E.-M. Charalampidou, S. A. Hall, S. Stanchits, G. Viggiani, and H. Lewis, "Shear-enhanced compaction band identification at the laboratory scale using acoustic and full-field methods," *Int. J. Rock Mech. Mining Sci.*, vol. 67, pp. 240–252, Apr. 2014, doi: [10.1016/j.ijrmm.2013.05.006](https://doi.org/10.1016/j.ijrmm.2013.05.006).
- [25] L. Hu, P. H. Winterfeld, P. Fakcharoenphol, and Y.-S. Wu, "A novel fully-coupled flow and geomechanics model in enhanced geothermal reservoirs," *J. Petroleum Sci. Eng.*, vol. 107, pp. 1–11, Jul. 2013, doi: [10.1016/j.petrol.2013.04.005](https://doi.org/10.1016/j.petrol.2013.04.005).
- [26] P. Jeanne, J. Rutqvist, C. Hartline, J. Garcia, P. F. Dobson, and M. Walters, "Reservoir structure and properties from geomechanical modeling and microseismicity analyses associated with an enhanced geothermal system at the geysers, California," *Geothermics*, vol. 51, pp. 460–469, Jul. 2014, doi: [10.1016/j.geothermics.2014.02.003](https://doi.org/10.1016/j.geothermics.2014.02.003).
- [27] I. Tomac and M. Sauter, "A review on challenges in the assessment of geomechanical rock performance for deep geothermal reservoir development," *Renew. Sustain. Energy Rev.*, vol. 82, pp. 3972–3980, Feb. 2018, doi: [10.1016/j.rser.2017.10.076](https://doi.org/10.1016/j.rser.2017.10.076).
- [28] A. Gens, B. Garitte, S. Olivella, and J. Vaunat, "Applications of multiphysical geomechanics in underground nuclear waste storage," *Eur. J. Environ. Civil Eng.*, vol. 13, nos. 7–8, pp. 937–962, Sep. 2009, doi: [10.1080/19648189.2009.9693162](https://doi.org/10.1080/19648189.2009.9693162).
- [29] S. Levasseur, F. Collin, R. Charlier, and D. Kondo, "On micromechanical damage modeling in geomechanics: Influence of numerical integration scheme," *J. Comput. Appl. Math.*, vol. 246, pp. 215–224, Jul. 2013, doi: [10.1016/j.cam.2012.05.022](https://doi.org/10.1016/j.cam.2012.05.022).
- [30] R. A. Ketcham and W. D. Carlson, "Acquisition, optimization and interpretation of X-ray computed tomographic imagery: Applications to the geosciences," *Comput. Geosci.*, vol. 27, no. 4, pp. 381–400, 2001, doi: [10.1016/S0098-3004\(00\)00116-3](https://doi.org/10.1016/S0098-3004(00)00116-3).
- [31] K. Singh, H. Menke, M. Andrew, Q. Lin, C. Rau, M. J. Blunt, and B. Bijeljic, "Dynamics of snap-off and pore-filling events during two-phase fluid flow in permeable media," *Sci. Rep.*, vol. 7, no. 1, pp. 1–13, Dec. 2017, doi: [10.1038/s41598-017-05204-4](https://doi.org/10.1038/s41598-017-05204-4).
- [32] E. Stavropoulou, E. And , E. Roubin, N. Lenoir, A. Tengattini, M. Briffaut, and P. B esuelle, "Dynamics of water absorption in callovo-oxfordian claystone revealed with multimodal X-ray and neutron tomography," *Frontiers Earth Sci.*, vol. 8, p. 6, Mar. 2020.
- [33] H. Lewis, S. Zihms, G. Couples, E. M. Charalampidou, S. Hall, E. Tudisco, and D. Atkins, "Use of neutron radiography and tomography to identify fracture network connectivity in low permeability carbonates," in *Proc. 23rd and 28th EGU Gen. Assem.*, Vienna, Austria, Apr. 2017, p. 19489.
- [34] J. Blanche, D. Flynn, H. Lewis, G. D. Couples, J. Buckman, C. Bailey, and T. Tilford, "Analysis of sandstone pore space fluid saturation and mineralogy variation via application of monostatic K-band frequency modulated continuous wave radar," *IEEE Access*, vol. 6, pp. 44376–44389, 2018, doi: [10.1109/access.2018.2863024](https://doi.org/10.1109/access.2018.2863024).
- [35] J. Holmgren, M. Sturm, N. E. Yankielun, and G. Koh, "Extensive measurements of snow depth using FM-CW radar," *Cold Regions Sci. Technol.*, vol. 27, no. 1, pp. 17–30, Feb. 1998.
- [36] H.-P. Marshall and G. Koh, "FMCW radars for snow research," *Cold Regions Sci. Technol.*, vol. 52, no. 2, pp. 118–131, Apr. 2008, doi: [10.1016/j.coldregions.2007.04.008](https://doi.org/10.1016/j.coldregions.2007.04.008).
- [37] N. Galin, A. Worby, R. Masson, G. Brooker, C. Leuschen, S. P. Gogineni, and P. Jansen, "2–8 GHz FMCW radar for estimating snow depth on antarctic sea ice," in *Proc. Int. Conf. Radar, Adelaide, SA, Australia*, Sep. 2008, pp. 276–281, doi: [10.1109/RADAR.2008.4653931](https://doi.org/10.1109/RADAR.2008.4653931).
- [38] N. Galin, A. Worby, T. Markus, C. Leuschen, and P. Gogineni, "Validation of airborne FMCW radar measurements of snow thickness over sea ice in antarctica," *IEEE Trans. Geosci. Remote Sens.*, vol. 50, no. 1, pp. 3–12, Jan. 2012, doi: [10.1109/tgrs.2011.2159121](https://doi.org/10.1109/tgrs.2011.2159121).
- [39] J. Blanche, J. Buckman, H. Lewis, D. Flynn, and G. Couples, "Frequency modulated continuous wave analysis of dynamic load deformation in geomaterials," in *Proc. 4th-7th Offshore Technol. Conf.*, Houston, TX, USA, May 2020, pp. 1–21, doi: [10.4043/30479-MS](https://doi.org/10.4043/30479-MS).
- [40] J. Blanche, D. Flynn, H. Lewis, G. Couples, and R. Cheung, "Analysis of geomaterials using frequency modulated continuous wave radar in the X-band," in *Proc. IEEE 26th Int. Symp. Ind. Electron. (ISIE)*, Edinburgh, U.K., Jun. 2017, pp. 19–21, doi: [10.1109/ISIE.2017.8001446](https://doi.org/10.1109/ISIE.2017.8001446).
- [41] J. Blanche, D. Flynn, H. Lewis, G. Couples, and R. Cheung, "Analysis of geomaterials using frequency modulated continuous wave radar in the X-band," presented at the IEEE 26th Int. Symp. Ind. Electron. (ISIE), London, U.K., Jun. 2017, pp. 13–16.
- [42] A. Tengattini, N. Lenoir, E. And , B. Giroud, D. Atkins, J. Beaucour, and G. Viggiani, "NeXT-grenoble, the neutron and X-ray tomograph in grenoble," *Nucl. Instrum. Methods Phys. Res. A, Accel. Spectrom. Detect. Assoc. Equip.*, vol. 968, Jul. 2020, Art. no. 163939, doi: [10.1016/j.nima.2020.163939](https://doi.org/10.1016/j.nima.2020.163939).

[43] J. H. Schön, *Physical Properties of Rocks: A Workbook* (Handbook of Petroleum Exploration and Production). Oxford, U.K.: Elsevier, 2011.

[44] W. J. Duffin, "Electromagnetic waves," in *Electricity and Magnetism*, vol. 366, 4th ed. Berkshire, U.K.: McGraw-Hill, 1990, pp. 366–368.

[45] Marshall-Stancliffe. *Darney Carboniferous Sandstone Datasheet*. Accessed: May 19, 2016. [Online]. Available: <http://www.stancliffe.com/assets/Stancliffe/ProductInformation/PDFs/StoneTypes/Stancliffe-Stone-Darney-Sandstone.pdf>

[46] Marshall-Stancliffe. *Red St. Bees Permo-Triassic Sandstone Datasheet*. Accessed: May 19, 2016. [Online]. Available: <http://www.stancliffe.com/assets/Stancliffe/ProductInformation/PDFs/StoneTypes/Stancliffe-Stone-Red-St-Bees-Sandstone.pdf>

[47] M. E. Tucker, *Sedimentary Rocks in the Field, A Practical Guide*, 4th ed. Chichester, U.K.: Wiley-Blackwell, 2011, p. 275.

[48] N. Lenoir, M. Bornert, J. Desrues, P. Bésuelle, and G. Viggiani, "Volumetric digital image correlation applied to X-ray microtomography images from triaxial compression tests on argillaceous rock," *Strain*, vol. 43, no. 3, pp. 193–205, Aug. 2007, doi: [10.1111/j.1475-1305.2007.00348.x](https://doi.org/10.1111/j.1475-1305.2007.00348.x).

[49] H. Lewis, G. D. Couples, A. Tengattini, J. Buckman, E. Tudisco, M. Etxegarai, S. Zihms, G. Viggiani, and S. A. Hall, "Interactions between imbibition and pressure-driven flow in a heterogeneous porous rock sample: Direct 3D observations and interpretation of water-air and water-water displacements," in *Transport in Porous Media*. Springer, 2020.

[50] J. Schindelin, I. Arganda-Carreras, E. Frise, V. Kaynig, M. Longair, T. Pietzsch, S. Preibisch, C. Rueden, S. Saalfeld, B. Schmid, J.-Y. Tinevez, D. J. White, V. Hartenstein, K. Eliceiri, P. Tomancak, and A. Cardona, "Fiji: An open-source platform for biological-image analysis," *Nature Methods*, vol. 9, no. 7, pp. 676–682, Jul. 2012, doi: [10.1038/nmeth.2019](https://doi.org/10.1038/nmeth.2019).

[51] M. A. Richards, *Fundamentals of Radar Signal Processing*, 2nd ed. New York, NY, USA: McGraw-Hill, 2014.



**JAMIE BLANCHE** (Member, IEEE) received the B.Sc. degree (Hons.) in physics with environmental science and the M.Sc. degree in petroleum geoscience from Heriot-Watt University, in 2003 and 2014, respectively. He is currently a Research Associate working on non-invasive sensing methodologies for laboratory-based geomechanical monitoring. He acquired upstream petroleum industry experience prior to achieving the M.Sc. degree. Joining the Smart Systems Group, in April 2015, his research interest is the novel use of radar sensing to determine in situ flow characteristics within deformed geomaterials, serving as a platform for preliminary work in real-time sensing within an extreme environment and a departure from current practices of post-failure analysis.

to determine in situ flow characteristics within deformed geomaterials, serving as a platform for preliminary work in real-time sensing within an extreme environment and a departure from current practices of post-failure analysis.



**HELEN LEWIS** received the B.Sc. (A.R.S.M.) degree in geology from Imperial College London, the M.Sc. (D.I.C.) degree in structural geology and rock mechanics from the University of London, and the Ph.D. degree from the University of Glasgow. She is currently an Associate Professor with the Institute of Geoenergy Engineering, Heriot-Watt University. Her research is based on incorporating quantitative geomechanics into structural geology. Her focus is twofold: linked

geomechanics and flow in developing geological structures at the sub-mm to the reservoir scale and laboratory-based rock, and flow system testing, particularly with embedded sensor systems. She has worked extensively with geomechanical simulation tools of various types, has extensive experience of fracture networks and their evolution, and is currently involved in a range of projects on characterizing, measuring, and modelling rocks, including X-ray and neutron tomography plus radar detections, some concurrently.



**GARY D. COUPLES** received the B.S. degree from Texas A&M University, in 1974, the M.A. degree from Rice University, in 1977, and the Ph.D. degree from Texas A&M University, in 1986. He is currently a Professor of geomechanics with the Institute of Geoenergy Engineering, Heriot-Watt University, Edinburgh, Scotland, where he works at the engineering-geology interface. He worked at Cities Service Company, Tulsa, and Amoco, Denver, and ran a consultancy before joining the

academic world, in 1989, first at the University of Glasgow, Scotland, before moving to Heriot-Watt University, in 1998. He teaches on three master's courses at Heriot-Watt University (lecturing to engineers and geoscientists) and also on a geomechanics master's programme at Joseph Fourier University, Grenoble, France. His research links geomechanical effects to their consequences. He was an SPE Distinguished Lecturer speaking on geomechanical issues in fractured reservoirs, from 2013 to 2014. He uses textural analysis and digital rocks in an effort to understand how rock properties are controlled by their depositional, diagenetic, and deformation histories.



**JIM BUCKMAN** is currently a Research Fellow with the Institute of Geoenergy Engineering, Heriot-Watt University, where he manages the scanning electron microscope (SEM) facility. He has a background in geological sciences and undertakes a range of SEM-based research into mudrocks, sandstones, carbonates, biological materials, wettability, and develops microscope techniques involving automation and analysis.



**NICOLAS LENOIR** is currently a CNRS Research Engineer working at the Laboratoire 3SR, Grenoble, France, a laboratory specialized in geomechanics, and the Institut Laue-Langevin (ILL), an international institute for neutron research, Grenoble. He has a background in geomechanics and works on the development of lab and large instrument tomographs, both X-ray and neutron. He also develops sample environments for *in situ* 3-D imaging and undertakes

tomograph-based research into different domains, mainly geomechanics, material sciences, and plants.



**ALESSANDRO TENGATTINI** is currently the Chair of the Université Grenoble Alpes/Institut Laue-Langevin (UGA/ILL) consortium on imaging for mechanics. He is also an instrument developer and is responsible for NeXT-Grenoble (Neutron and X-ray Tomograph) at the ILL. He is an expert in imaging and image analysis, with a background on the interface between full-field measurements and analytic/numerical models, with particular focus on Cemented Granular Materials.



**DAVID FLYNN** (Member, IEEE) received the B.Eng. degree (Hons.) in electrical and electronic engineering, the M.Sc. degree (Hons.) in microsystems, and the Ph.D. degree in microscale magnetic components from Heriot-Watt University, Edinburgh, in 2002, 2003, and 2007, respectively. He is currently an Eminent Overseas Professor with Nagasaki University, and a Professor with the Smart Systems Group, Heriot-Watt University. He is the Founder of the Smart

Systems Group (SSG), Heriot-Watt University, the activities of the SSG involve multidisciplinary expertise in sensor technologies, data analysis, and systems engineering, to create predictive and prescriptive analysis of systems. He is an IET Scholar. He teaches smart system integration, electrical engineering, and energy systems. He was a recipient of the Institute of Engineering and Technology (IET) Leslie H. Paddle Prize.

...